Journal of Applied Physics

RESEARCH ARTICLE | DECEMBER 24 2024

Exploring magnetism, topology, and magnetoresistance in rare-earth-based compound GdAuSn: *Ab initio* study

Sumit Mondal ; Jaspreet Singh ; V. Kanchana

J. Appl. Phys. 136, 243902 (2024)
https://doi.org/10.1063/5.0243956

Journal of Applied Physics ARTICLE pubs.aip.org/aip/jap

Exploring magnetism, topology, and magnetoresistance in rare-earth-based compound GdAuSn: *Ab initio* study

Cite as: J. Appl. Phys. **136**, 243902 (2024); doi: 10.1063/5.0243956
Submitted: 15 October 2024 · Accepted: 10 December 2024 ·
Published Online: 24 December 2024

Sumit Mondal,[1] Jaspreet Singh,[2] and V. Kanchana[2,a)]

AFFILIATIONS

[1]Department of Physics and Astrophysics, Central University of Haryana, Jant-Pali, 123031 Mahendergarh, Haryana, India
[2]Department of Physics, Indian Institute of Technology Hyderabad, Kandi, 502285 Sangareddy, Telangana, India

[a)]**Author to whom correspondence should be addressed:** kanchana@phy.iith.ac.in

ABSTRACT

Rare-earth intermetallics, especially Gd-based compounds, are of great interest due to their diverse magnetic ground states and intriguing topological properties. Using first-principles calculations, we investigate the magnetic, electronic, and phononic properties of GdAuSn. Our results identify the *C*-type antiferromagnetic configuration as the lowest energy state, with a critical temperature of 25 K estimated using the Heisenberg spin model and mean-field approximation. The electronic band structure reveals nodal surfaces and Dirac points, highlighting the material's non-trivial topology. In the magnetically ordered state, GdAuSn exhibits positive transverse magnetoresistance, increasing to ∼25% at 3.5 T and 10 K, with Hall resistivity analysis confirming electron-dominated transport. Additionally, phonon dispersion analysis uncovers topological phononic states with nodal surfaces. These findings provide insights into the interplay of magnetism, topology, and transport in GdAuSn, establishing its potential for fundamental research and topological antiferromagnetic spintronics.

I. INTRODUCTION

The intricate relationship between the electronic configuration and topology within materials guarantees a wide range of topological conditions. These encompass diverse states such as topological semimetals, topological insulators, and topological superconductors.[1–6] Topological semimetals are presently garnering significant interest within the topological materials field, owing to their promise for advanced industrial applications and as avenues for pioneering fundamental scientific studies.[1,3,7] Extensive research has delved into the topological states present in nonmagnetic materials, which adhere to time reversal symmetry ($\mathscr{T}$).[8–10] However, in magnetic systems, specific topological classes undergo significant transformations due to the absence of $\mathscr{T}$, resulting in diverse topological states. These topological non-trivialities are protected by certain crystalline or space or point symmetry groups. Magnetic materials have been observed to manifest various topological insulating states, Weyl points, and Dirac points.[11–18] These semimetals exhibit distinctive responses to both electric and magnetic fields and feature symmetry-protected band intersections between valence and conduction states. Their transport properties include a high carrier mobility, an extremely large magnetoresistance (MR), and a negative longitudinal MR.[19–22]

Within this framework, hexagonal ternary rare earth compounds have garnered significant attention owing to their potential to manifest diverse topological states. Of particular interest are materials that exhibit an intricate interplay between topology and magnetism. For instance, strongly correlated Yb-based compounds such as YbCdX (X = Ge and Sn) have been found to show interesting topological and magnetotransport properties.[23,24] Among these compounds, Eu- and Gd-based intermetallics stand out due to the presence of Gd^{3+} and Eu^{2+} oxidation states, characterized by a half-filled *f* shell with electron configuration $4f^7$, making them particularly intriguing. The magnetic properties of these compounds originate from the *f* orbitals, while the low-energy bands around the Fermi level arise from the dispersive *s* or *p* orbitals of other constituents. This configuration helps in clarifying topological features and improving carrier mobility. For example, the antiferromagnetic (AFM) Dirac semimetal EuAgAs displays a chiral

anomaly induced negative longitudinal MR and a significant topological Hall effect.[25] Magnetotransport and electronic band structure analyses have revealed substantial negative MR in EuAuAs, where a Dirac nodal line is present.[16] In Gd-based compounds, GdAgGe exhibits positive transverse MR, which increases with decreasing temperature and increasing field, featuring a nodal line with drumhead surface states associated with a nonzero Berry phase.[17] Another interesting compound, GdAuGe, demonstrates large positive MR and significant anomalous Hall conductivity at low temperatures, accompanied by the presence of a Dirac nodal line.[18]

In this study, we have explored the physical characteristics of GdAuSn, a member of a diverse group of ternary intermetallics featuring Gd, a rare earth element, and Au, a transition element. GdAuSn crystallizes in a hexagonal LiGaGe-type crystal structure with the space group $P6_3mc$.[26] The magnetism of GdAuSn was initially investigated by Oesterreicher through ac-susceptibility measurements, revealing an AFM ordering below the Neel temperature, $T_N = 35$ K.[27] Recent studies have reported slightly different T_N values of 23,[28] 26,[29] and 25 K.[30] Here, employing first-principles calculations, we have delved into the structural, magnetic, electronic, and dynamic properties of GdAuSn. Our investigation has unveiled the ground state magnetic configuration and determined exchange interactions using the Heisenberg spin model. We found that the ground state of GdAuSn exhibits a *C*-type AFM order with $T_N = 25$ K, consistent with experimental observations.[30] Electronic band structure analysis has revealed the presence of nodal surfaces in the absence of spin-orbit coupling (SOC) and a Dirac point upon including SOC. The non-trivial nature of our compound has been corroborated through the calculation of the Z_2 invariant. Additionally, GdAuSn displays topological features in its phonon dispersion. Our findings suggest that GdAuSn holds promise as a candidate for an AFM topological semimetal, encompassing both electron and phonon topology.

The organization of this paper is as follows: Sec. II provides a detailed description of the computational techniques employed. Following that, in Sec. III A, there is an in-depth discussion of the structural and magnetic properties. Section III B is dedicated to presenting the exchange interactions. The discussion on electronic properties is given in Sec. III C. The magnetoresistance explanations are provided in Sec. III D, and topological phonon properties can be found in Sec. III E. Finally, the paper is concluded in Sec. IV with a summary of our findings.

II. COMPUTATIONAL DETAILS

Using the Vienna *Ab Initio* Simulation Package (VASP), we conducted thorough geometry optimizations of the compound employing the generalized gradient approximation GGA-PBE.[31,32] The results obtained with GGA-PBE closely match experimental parameters. Our computations strictly adhere to self-consistency principles, ensuring energy and force convergence to within 10^{-6} eV and 10^{-2} eV Å^{-3}, respectively. We selected a $6 \times 12 \times 6$ *k*-mesh to generate a unique *k*-mesh within the irreducible Brillouin zone (BZ) using the Monkhorst–Pack approach.[33] Integration of the BZ is carried out using the tetrahedron approach, with an energy cutoff point set at 500 eV. To account for the correlation effects of Gd-*f* states, a Hubbard parameter (U) of 6 eV was employed.[17,18,34,35] For phonon dispersion computations, we employed the density functional perturbation method in VASP, along with Phonopy.[36] Phonon calculations were performed using a dense *k*-mesh ($12 \times 24 \times 12$) and a 10^{-8} eV energy convergence criterion. To assess the topological nature, we integrated the tight-binding Hamiltonian with the Wannier90 package.[37] The topological properties of the compound, as per the tight-binding model, were investigated utilizing the iterative Green's function technique, available in the WANNIERTOOLS package.[38,39] Magnetoresistance was calculated by combining Boltzmann transport theory with the Fermi surface derived from first-principles calculations,[40] utilizing the open-source software package WANNIERTOOLS.[38]

III. RESULTS AND DISCUSSION

A. Structural and magnetic properties

Gd, Au, and Sn atoms are located at Wyckoff positions 2a, 2b, and 2b, respectively, forming the unit cell of GdAuSn, comprising a total of six atoms. This compound crystallizes in a LiGaGe-type hexagonal structure with space group $P6_3mc$ (186), as depicted in Fig. 1(a). Additionally, it exhibits twofold screw rotational symmetry, denoted as $S_{2z} = \{C_{2z}|00\frac{1}{2}\}$, and features three vertical mirror planes, specifically $\widetilde{M}_{x\bar{y}} = \{M_{x\bar{y}}|00\frac{1}{2}\}$, $\widetilde{M}_{2xy} = \{M_{2xy}|00\frac{1}{2}\}$, and M_y.

In order to deduce the magnetic properties of our compound, we have considered different magnetic configurations. The magnetic cells are constructed by doubling the unit cell along the *a*-axis. The ferromagnetic (FM) and AFM (including *A*-, *C*-, *G*-type AFM) configurations are shown in Fig. 2. The calculated ground state energies for all these possible configurations are listed in Table I. Upon a thorough comparison of the energies attributed to various magnetic orders, facilitated by the PBE+U approach, Table I clearly highlights the *C*-AFM configuration as the one with the lowest energy. In the *C*-AFM configuration, we observe AFM coupling along the *a*-axis and FM coupling along the *b* and *c* axes. To further corroborate the spin orientations within the *C*-AFM case, we performed calculations for the ground state energies along different spin alignments such as [001], [010], [100], [011], [101], and [110]. The configuration with spins aligned along the [001] direction yields the minimum ground state energy.

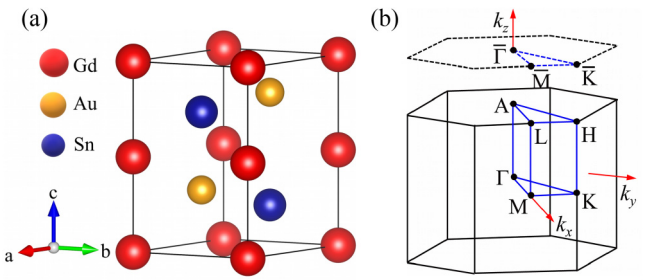

FIG. 1. (a) The crystal structure of GdAuSn. (b) The irreducible Brillouin zone of the bulk along with the (001) projected surface.

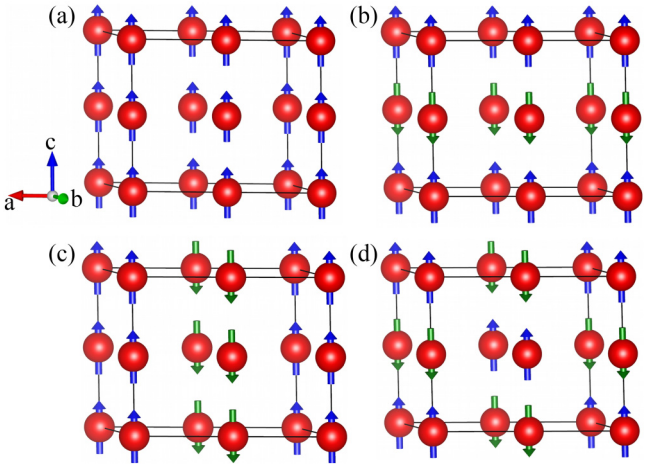

FIG. 2. Magnetic configurations for 2 × 1 × 1 supercell of GdAuSn with Gd spins. (a) FM, (b) *A*-AFM, (c) *C*-AFM, and (d) *G*-AFM. Blue and green arrows denote the spin-up and spin-down, respectively.

B. Exchange interaction

To comprehend the inherent magnetic properties at the ground state level, we harnessed the capabilities of the DFT to simulate an array of magnetic spin configurations. Within the realm of magnetic spin alignments, our exploration encompassed the FM, *A*-AFM, *C*-AFM, and *G*-AFM, as visually represented in Fig. 2. The exchange interactions can be approximated by correlating the total energies of different spin configurations obtained through DFT with the underlying Heisenberg spin model. This correlation involves expressing the Heisenberg spin model as

$$H = -\frac{1}{2}\sum_{ij} J_{ij}\mathbf{S}_i\mathbf{S}_j, \tag{1}$$

where J_{ij} represents the exchange interaction between sites i and j and $\mathbf{S}_{i(j)}$ denotes the respective spin at those sites. Figure 2 illustrates the different magnetic arrangements that were employed for the computation of exchange constants. The total energies for four formula units can be stated as follows using the Heisenberg Hamiltonian for all magnetic configurations,

$$F = -\frac{1}{2}S^2[8J_1 + 24J_2], \tag{2}$$

TABLE I. Calculated energies of different magnetic configurations (in meV) with the reference energy considered to be 0 meV.

Configuration	FM	*A*-AFM	*C*-AFM	*G*-AFM
Energy (meV)	22.52	12.43	0	11.22

$$A = -\frac{1}{2}S^2[-8J_1 + 24J_2], \tag{3}$$

$$C = -\frac{1}{2}S^2[8J_1 - 8J_2], \tag{4}$$

$$G = -\frac{1}{2}S^2[-8J_1 - 8J_2], \tag{5}$$

where F, A, C, and G represent FM, A-AFM, C-AFM, and G-AFM, respectively. The exchange constants J_1 and J_2 correspond to interactions between spins at varying distances: first-nearest-neighbor and second-nearest-neighbor. These exchange constants can be obtained from Eq. (5) using

$$J_1 = -\frac{1}{8S^2}[C - G], \tag{6}$$

$$J_2 = -\frac{1}{32S^2}[F - C], \tag{7}$$

where we assume $S = \frac{7}{2}$, in accordance with the calculated magnetic moment per Gd ion. The calculated exchange interactions for GdAuSn are $J_1 = 0.172$ and $J_2 = -0.585$ meV. The results indicate that an FM coupling is favored along the c direction and AFM coupling in ab plane.

The critical (Neel) temperature can be estimated using the mean-field expression as[27]

$$T_N = \frac{S(S+1)}{3k_B}\left(\sum_i z_i J_i\right), \tag{8}$$

where k_B represents the Boltzmann constant and z_i represents the number of closest neighbors. Here, $z_1 = 2$ and $z_2 = 6$ are the number of nearest neighbors in GdAuSn. The determined value of T_N is 25 K, which is consistent with the experimental result.[30]

C. Electronic properties

We calculated the total density of states (DOS) and the projected density of states (PDOS) for the *C*-AFM case to elucidate the behavior of Gd, Au, and Sn elements. The results are visualized in Fig. 3(a). In the valence band region, contributions from Gd, Au, and Sn atoms are approximately equal. However, in both spin channels, the conduction region is predominantly governed by Gd. We also explored the properties of electronic band structure. Figure 3(b) illustrates the electronic band structure, with the spin-up bands (in red) and the spin-down bands (in blue). Both the electronic band structure and density of states indicate that GdAuSn displays metallic characteristics.

In the absence of SOC, the electronic band structure shows interesting band crossings and degenerate bands. We can see that the doubly degenerate bands are present along k-path A-L-H-A on the $k_z = 0.5$ plane, as shown in Fig. 3(b). In fact, we check that all the bands in the $k_z = 0.5$ plane are doubly degenerate. The degeneracy is due to the linear crossing between two bands along

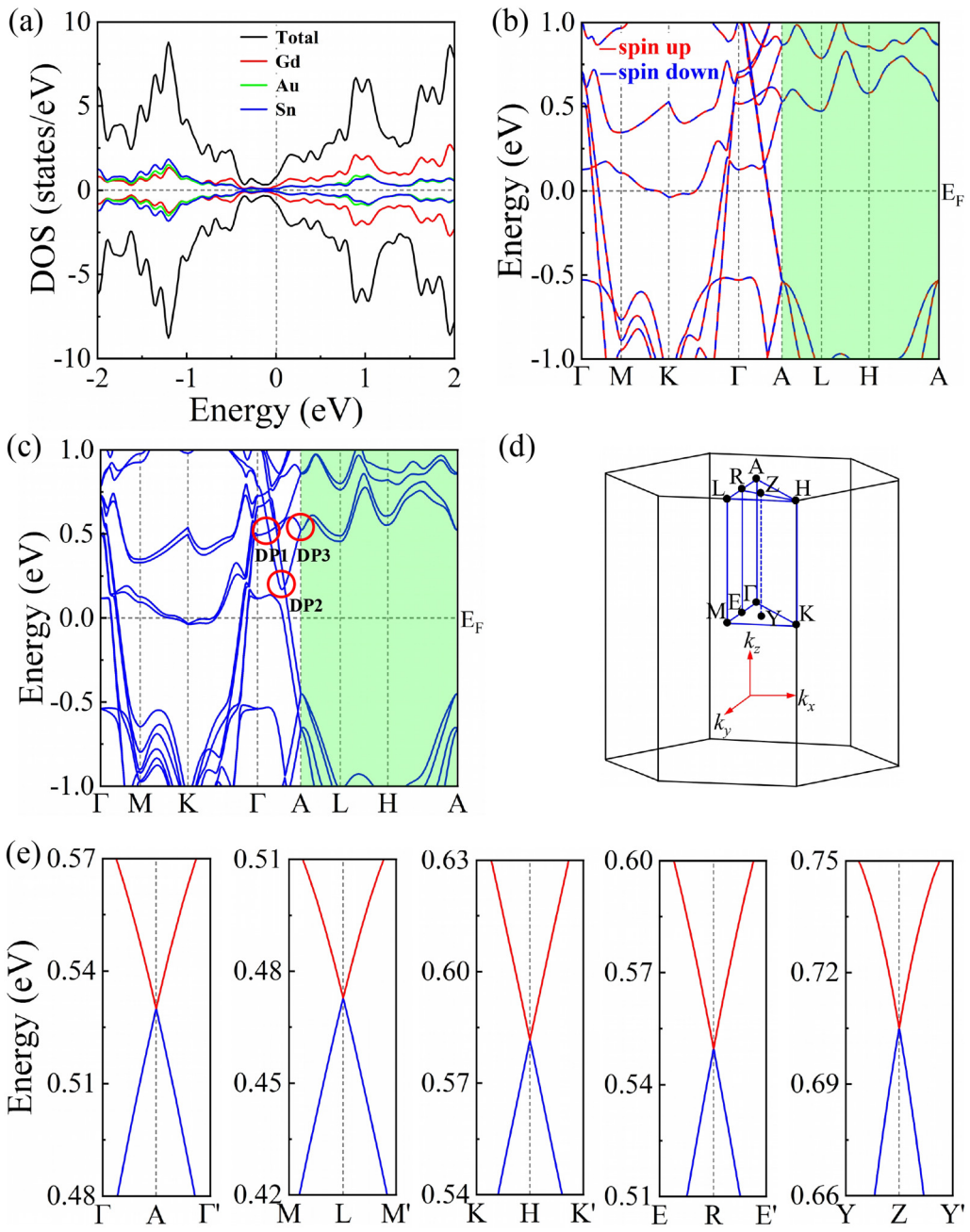

FIG. 3. (a) Total and projected density of states of GdAuSn. (b) Electronic band structure along Γ-M-K-Γ-A-L-H-A path without SOC. (c) Electronic band structure with SOC. (d) The BZ of the bulk with selected *k*-points. In (d), R and E are the midpoints of the paths A-L and Γ-M, respectively, while Z and Y denote the midpoints of the planes A-L-H-A and Γ-M-K-Γ, respectively. (e) The calculated band structure along the five paths perpendicular to the $k_z = \pi$ plane.

the k_z direction. The doubly degenerate band on the $k_z = 0.5$ plane may be part of the nodal surface (NS). This NS is identified as a class-II NS, supported by a detailed symmetry analysis. The space group of our investigated system possesses the S_{2z} symmetry, which is a non-symmorphic symmetry involving a half-translation along its rotation axis. In momentum space, S_{2z} reverses k_x and k_y while leaving k_z unchanged. In the absence of SOC, the relation $(S_{2z})^2 = T_{001} = e^{-ik_z}$ holds, where T_{001} denotes a translation along the z

axis by one lattice constant. The $\mathcal{T}$ operator, being antiunitary, reverses k and satisfies $\mathcal{T}^2 = 1$. As a result, the combined symmetry operator $\mathcal{T}S_{2z}$ is antiunitary and acts only to invert k_z. Since $\mathcal{T}$ and S_{2z} commute, the operator $\mathcal{T}S_{2z}$ satisfies $(\mathcal{T}S_{2z})^2 = e^{-ik_z}$. Crucially, every point on the $k_z = \pi$ plane is invariant under $\mathcal{T}S_{2z}$. According to the preceding relation, the antiunitary symmetry satisfies $(\mathcal{T}S_{2z})^2 = -1$ on the entire plane, leading to a twofold Kramers degeneracy at all points within this plane. However, this degeneracy is generally lifted outside the plane due to the loss of symmetry protection, resulting in the emergence of a class-II NS at the $k_z = \pi$ plane. To further understand the formation mechanism of the NS in the k_z = 0.5 plane, we have also calculated the band dispersions along several k-paths perpendicular to the plane [see Fig. 3(d)]. The results are shown in Fig. 3(e). The generic k-points Y and Z refer to the center positions of the triangles K-Γ-M and H-A-L. We have also added two high-symmetry k-points R and E at the midpoint of the A-L and Γ-M lines. We can clearly observe that the two bands have a linear crossing along all these perpendicular k-paths. The analysis of the bands reveals a noteworthy observation: the point at which bands intersect along every k-path is consistently positioned at the midpoint of the path. The presence of this linear band crossing along k-paths perpendicular to the k_z = 0.5 plane serves as evidence for the twofold band degeneracy occurring between the valence and conduction bands at the k_z = 0.5 plane. The above results confirm that the bands on the k_z = 0.5 plane are NSs, which are protected by the combination of $\mathcal{T}$ and S_{2z} symmetries.

We have done a thorough analysis of the band crossings along the Γ-A direction (corresponding to the k_z axis) in the presence of SOC. It is worth noting that each band along the k_z axis (specifically along the Γ-A path) exhibits double degeneracy due to the anticommutation relation between S_{2z} and M_x symmetries. We can see that three distinct twofold degenerate bands intersect at specific points denoted as DP1, DP2, and DP3. DP1 and DP2 emerge as a result of accidental band crossings and are located precisely on the rotation axis. Conversely, DP3 represents an essential band crossing

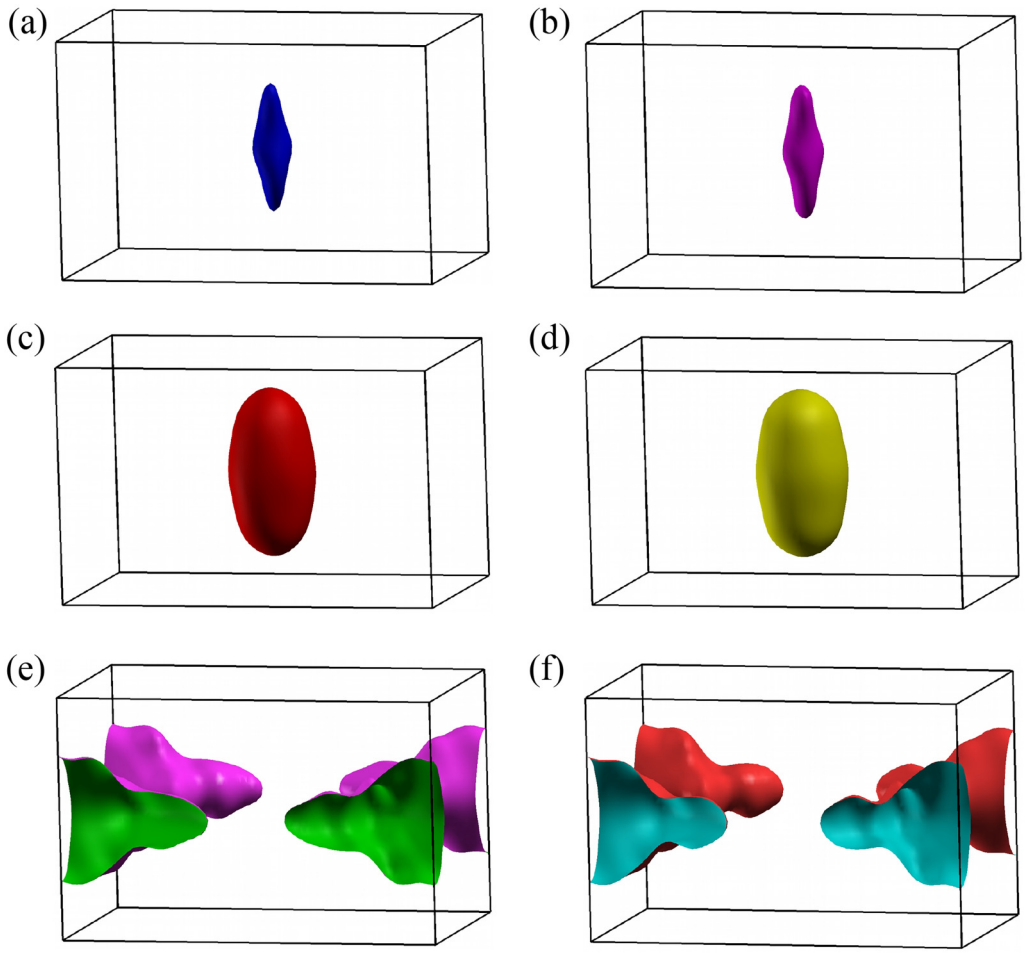

FIG. 4. (a–f) The Fermi surfaces of GdAuSn in the presence of SOC.

point, dictated by the non-symmorphic symmetries inherent in the space group. Consequently, all three band crossings along the Γ-A direction manifest as four-fold degenerate Dirac points. Significantly, Dirac band crossings are typically forbidden in non-centrosymmetric materials due to the breaking of inversion symmetry. However, our study reveals that GdAuSn stands out as a unique non-centrosymmetric system that exhibits Dirac points in its electronic structure. This distinct feature adds to its intriguing electronic properties. Taking into account the effective $\mathcal{T}$ symmetry, we computed the Z_2 invariants. The calculated Z_2 invariants, (0; 1 1 1), indicate that GdAuSn is a weak topological material.

Next, we have discussed the Fermi surface with the inclusion of SOC. The recent studies on Fermi surface topology signified its importance in magneto-transport properties like magnetoresistance.[40] The Fermi surface plots for six bands are shown in Fig. 4. All these Fermi surfaces exhibit electronic character due to the band crossing the Fermi level from the conduction band to the valence band. The first four closed Fermi surfaces are corresponding to the bands that cross the Fermi level around Γ and A points, which are shown in Figs. 4(a)–4(d). Next two Fermi plots are corresponding to the bands that cross the Fermi level around K point.

D. Magnetoresistance

The intriguing electronic properties of GdAuSn discussed earlier motivate us to investigate the effect of the magnetic field on its electrical resistivity using the Boltzmann transport theory within the relaxation time approximation. In this study, six bands crossing the Fermi level, all of which are electron-like as shown in Fig. 4, have been analyzed for their impact on total resistivity and MR. We calculated the Hall resistivity (ρ_{xy}) as a function of the magnetic field. Figure 5(a) presents the field-dependent ρ_{xy} data at

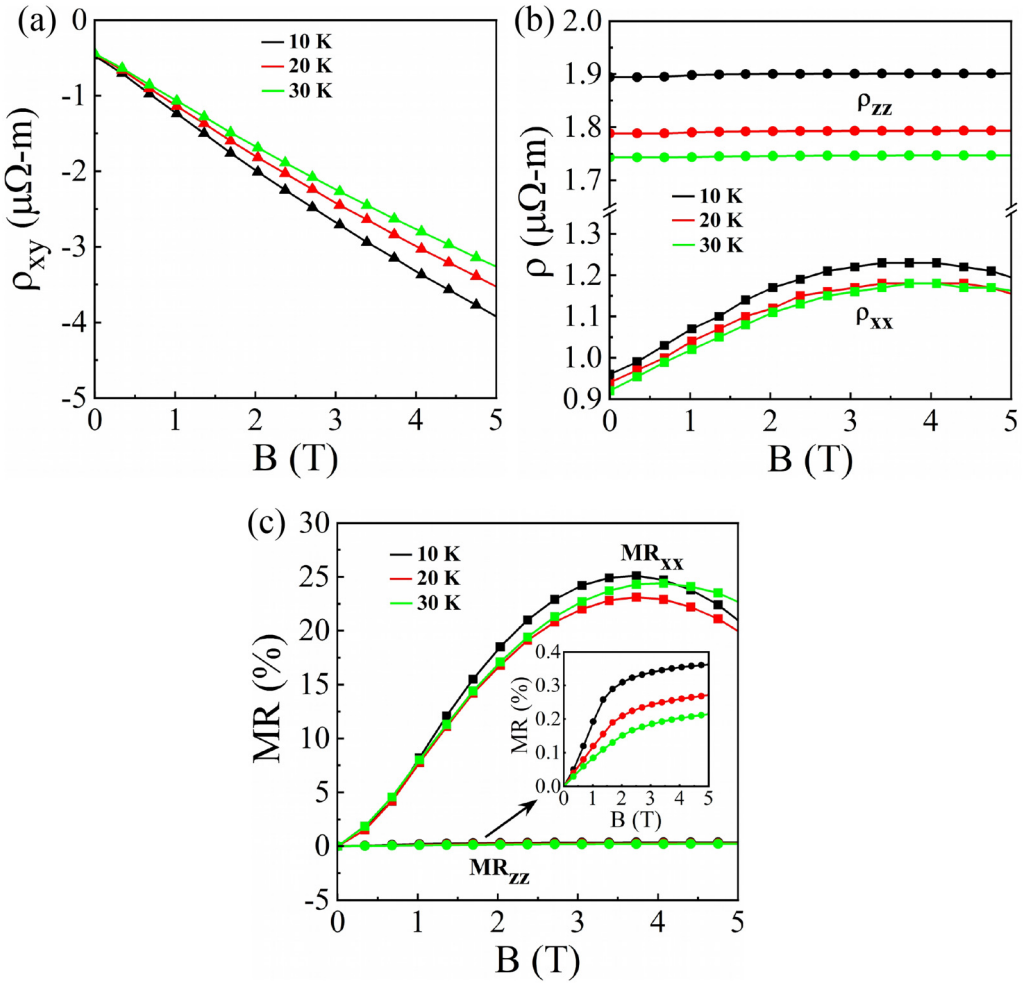

FIG. 5. (a) Hall resistivity, (b) the longitudinal (ρ_{zz}) and transverse (ρ_{xx}) electrical resistivity, and (c) the longitudinal (MR_{zz}) and transverse (MR_{xx}) magnetoresistance as a function of magnetic field. In (c), the inset figure presents MR_{zz}.

various temperatures ranging from 10 to 30 K. The ρ_{xy} data exhibit a negative linear dependence on the magnetic field, indicating the presence of electron charge carriers in the electrical transport of GdAuSn, which is consistent with our Fermi surface calculations. Next, we computed the electrical resistivity along the x and z directions to observe the transverse and longitudinal effects of the applied magnetic field. The calculated electrical resistivities, both transverse (ρ_{xx}) and longitudinal (ρ_{zz}), are presented in Fig. 5(b). It is evident that ρ_{zz} values are larger than ρ_{xx} across all temperatures, namely, 10, 20, and 30 K. The temperature-dependent resistivity exhibits a metallic-like increase in zero magnetic field. Furthermore, it is noticeable that ρ_{xx} increases with increasing magnetic field strength, but it begins to decrease after reaching a field strength of approximately 3.5 T. Conversely, the value of ρ_{zz} is observed to remain nearly constant with magnetic field strength.

The magnetic field-dependent MR corresponding to these resistivities is presented in Fig. 5(c). From Fig. 5(c), we can see that the transverse MR values (MR_{xx}) are higher than the longitudinal MR values (MR_{zz}). If we observe the variation of MR_{xx} with a change in magnetic field, initially it increases with an increase in field value and starts decreasing later on, while the values of MR_{zz} remain nearly constant. A similar positive trend in MR has been observed in the isostructural compound GdAuGe, known as a Dirac material.[18]

E. Phononic properties

To explore the dynamical stability of our compound, we conducted phonon dispersion calculations and generated a plot along the high-symmetry path [see Fig. 1(b)]. Figure 6(a) reveals that the acoustic branches predominantly resided in the positive frequency region, signifying the robust dynamical stability of GdAuSn. Due to the non-equivalent atomic masses of the constituents, we observed less interaction between the acoustic and optical modes in the phonon dispersion curve. To gain further insights into the atomic contributions to phonons, we computed the phonon density of states which is shown in Fig. 6(b). The resulting plot indicated that the low-frequency phonon modes were influenced by the Au atoms whereas the higher-frequency optical modes received contributions

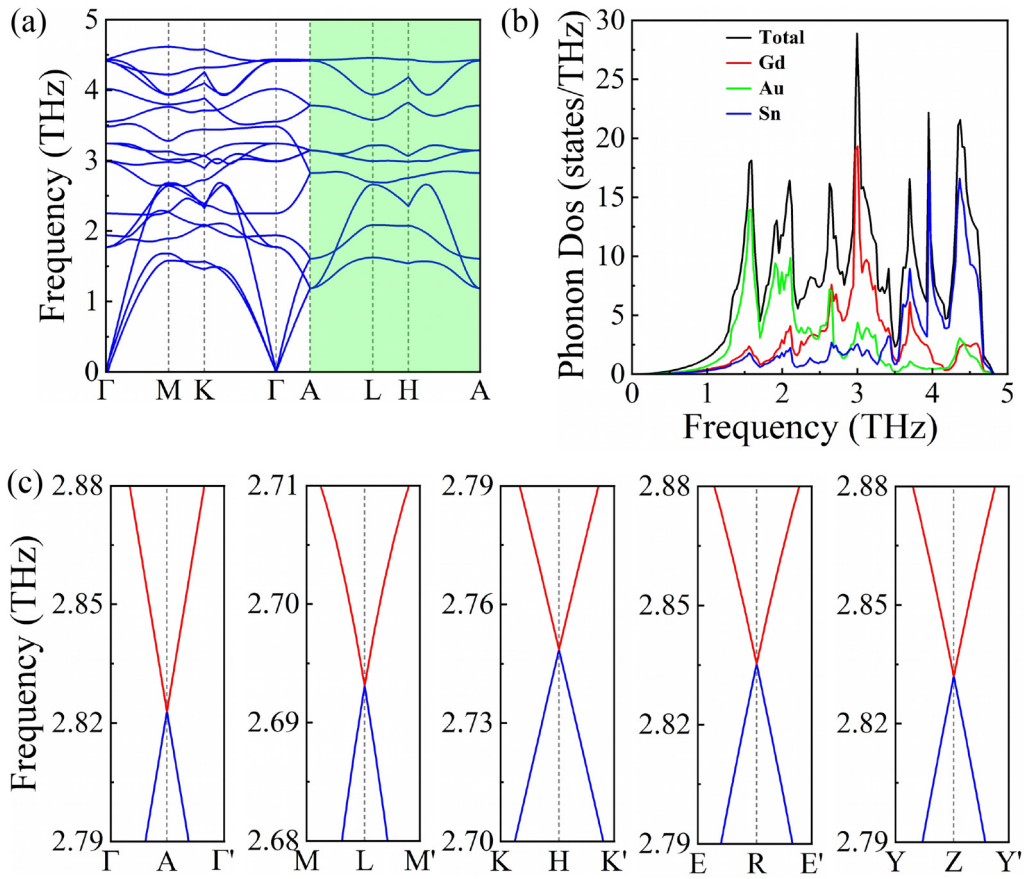

FIG. 6. (a) Phonon dispersion along the high-symmetry path. (b) Total and projected phonon density of states. (c) Phonon dispersion along the selected k-path as shown in Fig. 3(d).

from Sn atoms. The frequency region between the low- and high-frequency region mainly contributed by Gd atoms.

Similar to the electronic band structure, here also we can see the twofold band degeneracy along the $k_z = 0.5$ plane. To illustrate this phenomenon, we deliberately present the band dispersion along several k-paths perpendicular to the plane [see Fig. 3(d)]. The clear observation of the linear crossing on these selected paths confirms the presence of NSs along $k_z = 0.5$ plane. This observation aligns seamlessly with the previously mentioned argument that the antiunitary symmetry $\mathcal{T}S_{2z}$ plays a pivotal role in ensuring the presence of a nodal surface at the $k_z = 0.5$ plane.

IV. CONCLUSION

In summary, our study explores the fascinating properties of the rare-earth intermetallic compound GdAuSn through comprehensive computational analyses. We identify its C-type antiferromagnetic configuration with a critical temperature of 25 K. Our electronic analysis reveals topological features, including Dirac points and nodal surfaces, highlighting the compound's potential for novel electronic applications. Additionally, we investigate the magnetoresistance behavior, showing how external magnetic fields influence the material's transport properties. Phonon dispersion analysis uncovers topological nodal surfaces, while the calculated Z_2 invariants confirm the material as a non-trivial topological antiferromagnetic system. Overall, our findings contribute to the understanding of rare-earth-based intermetallic compounds and their potential applications in electronics and magnetism.

ACKNOWLEDGMENTS

S.M. would like to thank V.K. and IIT Hyderabad for providing various resources essential for this work. The authors J.S. and V.K. acknowledge the National Supercomputing Mission (NSM) for providing computing resources of PARAM SEVA at IIT Hyderabad. J.S. was supported through a CSIR scholarship. The authors express their gratitude for Project No. CRG/2022/005228.

AUTHOR DECLARATIONS

Conflict of Interest

The authors have no conflicts to disclose.

Author Contributions

Sumit Mondal: Conceptualization (equal); Data curation (equal); Formal analysis (equal); Investigation (equal); Software (equal); Validation (equal); Visualization (equal); Writing – original draft (equal). **Jaspreet Singh:** Conceptualization (equal); Data curation (equal); Formal analysis (equal); Investigation (equal); Methodology (equal); Software (equal); Validation (equal); Visualization (equal); Writing – original draft (equal). **V. Kanchana:** Conceptualization (equal); Project administration (equal); Supervision (equal); Writing – review & editing (equal).

DATA AVAILABILITY

The data that support the findings of this study are available from the corresponding author upon reasonable request.

REFERENCES

[1]N. P. Armitage, E. J. Mele, and A. Vishwanath, "Weyl and Dirac semimetals in three-dimensional solids," Rev. Mod. Phys. **90**, 015001 (2018).
[2]B. Yan and C. Felser, "Topological materials: Weyl semimetals," Annu. Rev. Condens. Matter Phys. **8**, 337–354 (2017).
[3]M. Z. Hasan and C. L. Kane, "Colloquium: Topological insulators," Rev. Mod. Phys. **82**, 3045–3067 (2010).
[4]K. Li, C. Li, J. Hu, Y. Li, and C. Fang, "Dirac and nodal line magnons in three-dimensional antiferromagnets," Phys. Rev. Lett. **119**, 247202 (2017).
[5]Q. Wang, Y. Xu, R. Lou, Z. Liu, M. Li, Y. Huang, D. Shen, H. Weng, S. Wang, and H. Lei, "Large intrinsic anomalous Hall effect in half-metallic ferromagnet $Co_3Sn_2S_2$ with magnetic Weyl fermions," Nat. Commun. **9**, 3681 (2018).
[6]E. Liu, Y. Sun, N. Kumar, L. Muechler, A. Sun, L. Jiao, S.-Y. Yang, D. Liu, A. Liang, Q. Xu, J. Kroder, V. Süß, H. Borrmann, C. Shekhar, Z. Wang, C. Xi, W. Wang, W. Schnelle, S. Wirth, Y. Chen, S. T. B. Goennenwein, and C. Felser, "Giant anomalous Hall effect in a ferromagnetic Kagome-lattice semimetal," Nat. Phys. **14**, 1125–1131 (2018).
[7]A. Bansil, H. Lin, and T. Das, "Colloquium: Topological band theory," Rev. Mod. Phys. **88**, 021004 (2016).
[8]M. G. Vergniory, L. Elcoro, C. Felser, N. Regnault, B. A. Bernevig, and Z. Wang, "A complete catalogue of high-quality topological materials," Nature **566**, 480–485 (2019).
[9]F. Tang, H. C. Po, A. Vishwanath, and X. Wan, "Comprehensive search for topological materials using symmetry indicators," Nature **566**, 486–489 (2019).
[10]T. Zhang, Y. Jiang, Z. Song, H. Huang, Y. He, Z. Fang, H. Weng, and C. Fang, "Catalogue of topological electronic materials," Nature **566**, 475–479 (2019).
[11]X. Wan, A. M. Turner, A. Vishwanath, and S. Y. Savrasov, "Topological semimetal and Fermi-arc surface states in the electronic structure of pyrochlore iridates," Phys. Rev. B **83**, 205101 (2011).
[12]G. Xu, H. Weng, Z. Wang, X. Dai, and Z. Fang, "Chern semimetal and the quantized anomalous Hall effect in $HgCr_2Se_4$," Phys. Rev. Lett. **107**, 186806 (2011).
[13]D. Zhang, M. Shi, T. Zhu, D. Xing, H. Zhang, and J. Wang, "Topological axion states in the magnetic insulator $MnBi_2Te_4$ with the quantized magnetoelectric effect," Phys. Rev. Lett. **122**, 206401 (2019).
[14]J. Li, Y. Li, S. Du, Z. Wang, B.-L. Gu, S.-C. Zhang, K. He, W. Duan, and Y. Xu, "Intrinsic magnetic topological insulators in van der Waals layered $MnBi_2Te_4$-family materials," Sci. Adv. **5**, eaaw5685 (2019).
[15]T. He, X. Zhang, Y. Liu, X. Dai, G. Liu, Z.-M. Yu, and Y. Yao, "Ferromagnetic hybrid nodal loop and switchable type-I and type-II Weyl fermions in two dimensions," Phys. Rev. B **102**, 075133 (2020).
[16]S. Malick, J. Singh, A. Laha, V. Kanchana, Z. Hossain, and D. Kaczorowski, "Electronic structure and physical properties of EuAuAs single crystal," Phys. Rev. B **105**, 045103 (2022).
[17]D. Ram, J. Singh, M. K. Hooda, O. Pavlosiuk, V. Kanchana, Z. Hossain, and D. Kaczorowski, "Electronic structure and physical properties of the candidate topological material GdAgGe," Phys. Rev. B **107**, 085137 (2023).
[18]D. Ram, J. Singh, M. K. Hooda, K. Singh, V. Kanchana, D. Kaczorowski, and Z. Hossain, "Multiple magnetic transitions, metamagnetism, and large magnetoresistance in GdAuGe single crystals," Phys. Rev. B **108**, 235107 (2023).
[19]C.-L. Zhang, S.-Y. Xu, I. Belopolski, Z. Yuan, Z. Lin, B. Tong, G. Bian, N. Alidoust, C.-C. Lee, S.-M. Huang, T.-R. Chang, G. Chang, C.-H. Hsu, H.-T. Jeng, M. Neupane, D. S. Sanchez, H. Zheng, J. Wang, H. Lin, C. Zhang, H.-Z. Lu, S.-Q. Shen, T. Neupert, M. Zahid Hasan, and S. Jia, "Signatures of the Adler–Bell–Jackiw chiral anomaly in a Weyl fermion semimetal," Nat. Commun. **7**, 10735 (2016).
[20]J. Xiong, S. K. Kushwaha, T. Liang, J. W. Krizan, M. Hirschberger, W. Wang, R. J. Cava, and N. P. Ong, "Evidence for the chiral anomaly in the Dirac semimetal Na_3Bi," Science **350**, 413–416 (2015).
[21]C. Shekhar, A. K. Nayak, Y. Sun, M. Schmidt, M. Nicklas, I. Leermakers, U. Zeitler, Y. Skourski, J. Wosnitza, Z. Liu, Y. Chen, W. Schnelle, H. Borrmann, Y. Grin, C. Felser, and B. Yan, "Extremely large magnetoresistance and ultrahigh

mobility in the topological Weyl semimetal candidate NbP," Nat. Phys. **11**, 645–649 (2015).
[22]T. Liang, J. Lin, Q. Gibson, S. Kushwaha, M. Liu, W. Wang, H. Xiong, J. A. Sobota, M. Hashimoto, P. S. Kirchmann, Z.-X. Shen, R. J. Cava, and N. P. Ong, "Anomalous Hall effect in $ZrTe_5$," Nat. Phys. **14**, 451–455 (2018).
[23]A. Laha, S. Malick, R. Singha, P. Mandal, P. Rambabu, V. Kanchana, and Z. Hossain, "Magnetotransport properties of the correlated topological nodal-line semimetal YbCdGe," Phys. Rev. B **99**, 241102 (2019).
[24]A. Laha, P. Rambabu, V. Kanchana, L. Petit, Z. Szotek, and Z. Hossain, "Experimental and theoretical study of the correlated compound YbCdSn: Evidence for large magnetoresistance and mass enhancement," Phys. Rev. B **102**, 235135 (2020).
[25]A. Laha, R. Singha, S. Mardanya, B. Singh, A. Agarwal, P. Mandal, and Z. Hossain, "Topological Hall effect in the antiferromagnetic Dirac semimetal EuAgAs," Phys. Rev. B **103**, L241112 (2021).
[26]S. Gupta and K. Suresh, "Review on magnetic and related properties of RTX compounds," J. Alloys Compd. **618**, 562–606 (2015).
[27]H. Oesterreicher, "Magnetic properties of GdCuSn and GdAuSn," J. Less Common Met. **55**, 131–133 (1977).
[28]K. Łatka, E. Görlich, W. Chajec, R. Kmieć, and A. Pacyna, "Crystal and magnetic properties of GdTSn compounds (T = Ag, Au)," J. Alloys Compd. **262**, 108–113 (1997).
[29]F. Casper, V. Ksenofontov, H. C. Kandpal, S. Reiman, T. Shishido, M. Takahashi, M. Takeda, and C. Felser, "Structure and properties of GdAuSn and the GdAuSn/MnAuSn system," Z. Anorg. Allg. Chem. **632**, 1273–1280 (2006).
[30]D. Ryan, J. Cadogan, V. Krylov, A. Legros, R. Rejali, and C. Boyer, "The magnetic structures of GdCuSn, GdAgSn and GdAuSn," J. Phys.: Condens. Matter **29**, 495804 (2017).
[31]G. Kresse and J. Furthmüller, "Efficiency of ab-initio total energy calculations for metals and semiconductors using a plane-wave basis set," Comput. Mater. Sci. **6**, 15–50 (1996).
[32]J. P. Perdew, K. Burke, and M. Ernzerhof, "Generalized gradient approximation made simple," Phys. Rev. Lett. **77**, 3865–3868 (1996).
[33]H. J. Monkhorst and J. D. Pack, "Special points for Brillouin-zone integrations," Phys. Rev. B **13**, 5188–5192 (1976).
[34]M. Petersen, J. Hafner, and M. Marsman, "Structural, electronic and magnetic properties of Gd investigated by DFT+ U methods: Bulk, clean and H-covered (0001) surfaces," J. Phys.: Condens. Matter **18**, 7021 (2006).
[35]Z. Li, H. Su, X. Yang, and J. Zhang, "Electronic structure of the antiferromagnetic topological insulator candidate GdBiPt," Phys. Rev. B **91**, 235128 (2015).
[36]X. Gonze and C. Lee, "Dynamical matrices, Born effective charges, dielectric permittivity tensors, and interatomic force constants from density-functional perturbation theory," Phys. Rev. B **55**, 10355–10368 (1997).
[37]G. Pizzi, V. Vitale, R. Arita, S. Blügel, F. Freimuth, G. Géranton, M. Gibertini, D. Gresch, C. Johnson, T. Koretsune *et al.*, "Wannier90 as a community code: New features and applications," J. Phys.: Condens. Matter **32**, 165902 (2020).
[38]Q. Wu, S. Zhang, H.-F. Song, M. Troyer, and A. A. Soluyanov, "WannierTools: An open-source software package for novel topological materials," Comput. Phys. Commun. **224**, 405–416 (2018).
[39]M. L. Sancho, J. L. Sancho, J. L. Sancho, and J. Rubio, "Highly convergent schemes for the calculation of bulk and surface Green functions," J. Phys. F: Met. Phys. **15**, 851 (1985).
[40]S. Zhang, Q. Wu, Y. Liu, and O. V. Yazyev, "Magnetoresistance from Fermi surface topology," Phys. Rev. B **99**, 035142 (2019).